




Bayesian learning for optimal control of quantum many-body states in optical latticesYan-Jun Xie ^{1,2,3} Han-Ning Dai ^{1,2,3,*} Zhen-Sheng Yuan,^{1,2,3} Youjin Deng ^{1,2,3,4} Xiaopeng Li,^{2,5,6}
Yu-Ao Chen,^{1,2,3} and Jian-Wei Pan^{1,2,3,†}¹*Hefei National Research Center for Physical Sciences at the Microscale and School of Physical Sciences,
University of Science and Technology of China, Hefei 230026, China*²*Shanghai Research Center for Quantum Science and CAS Center for Excellence in Quantum Information and Quantum Physics,
University of Science and Technology of China, Shanghai 201315, China*³*Hefei National Laboratory, University of Science and Technology of China, Hefei 230088, China*⁴*MinJiang Collaborative Center for Theoretical Physics, College of Physics and Electronic Information Engineering,
Minjiang University, Fuzhou 350108, China*⁵*State Key Laboratory of Surface Physics, and Department of Physics, Fudan University, Shanghai 200438, China*⁶*Shanghai Qi Zhi Institute, Shanghai 200030, China*

(Received 17 February 2022; accepted 1 July 2022; published 22 July 2022)

Strongly correlated quantum many-body states provide invaluable resources for state-of-the-art quantum information science, ranging from quantum simulation to quantum metrology. In this work, we propose a supervised machine learning algorithm for optimal control of quantum many-body atomic states in optical lattices by numerical simulations based on the Bayesian method of Gaussian process regression (GPR). We combine this method with the time evolving block decimation (TEBD) algorithm for the preparation of the Heisenberg antiferromagnetic state in a system of bosonic atoms confined with a one-dimensional optical lattice. The quantum many-body ground state of 80 atoms is efficiently optimized within a few hundred machine learning iterations, reaching a state fidelity above 96%. With a multistep learning strategy, we find the machine-learning-based optimal control method is scalable to large systems owing to its transferability. Its robustness against noise is demonstrated by considering imperfections that are typically present in optical lattice experiments. In the application of the GPR method to the preparation of the two-dimensional (2D) antiferromagnetic state, a state fidelity of 94% is reached for a 2D array of 6×6 spins through the time dependent variational principle (TDVP) algorithm, confirming the generalizability of our method. We further optimize the Hamiltonian ramping sequence crossing a quantum phase transition of the quantum XXZ spin chain with the exact diagonalization method, from which a control protocol for generating the long-sought atomic Greenberger-Horne-Zeilinger state is obtained. We believe the proposed optimal control method for quantum Hamiltonian ground-state preparation would benefit present ultracold-atom experiments in the study of strongly correlated many-body physics.

DOI: [10.1103/PhysRevA.106.013316](https://doi.org/10.1103/PhysRevA.106.013316)**I. INTRODUCTION**

Controlling and studying quantum many-body physics are an important research frontier in quantum information science and condensed-matter physics [1–5]. In the last few decades, quantum simulation has become a versatile tool to investigate quantum many-body phases and dynamics [6–8]. By engineering strongly correlated many-body systems, varieties of quantum Hamiltonians have been studied based on different platforms, such as cold atoms, ion traps, superconducting circuits, and photonic systems [9–15].

One major challenge in these platforms is preparing a quantum many-body state in a large Hilbert space with a dimensionality that scales exponentially with the system size. One standard approach to reach a quantum many-body ground state is via adiabatic time evolution. Specifically, one first prepares an isolated pure quantum state under an initial Hamiltonian, then changes the Hamiltonian while preserving

coherence so that the quantum state approaches the target state [16]. In experiment, the adiabatic passages can be optimized with the help of classical optimal control methods, such as the chopped random basis [17], gradient-ascent pulse engineering [18], and the quantum approximate optimization algorithm [19,20]. They have been successfully used in optimizing multiqubit quantum gates [21], controlling nuclear magnetic resonance [22], and solving the maximum 2-satisfiability (MAX-2-SAT) problems [23]. However, their performances are limited in multivariable optimization problems, especially when considering experimental constraints, such as time limitations and systematic noises [24,25].

An alternative approach is to optimize the coherent evolution through machine learning algorithms [26–29], which has been shown to be successful in treating large parameter space by exploiting a large amount of data. Several algorithms have been used for different platforms [30–32], and schemes have been proposed for ultracold atoms [33,34]. Specifically, Gaussian process regression (GPR) is a generic supervised learning method based on Bayes' rule, which can build a probabilistic model from training data [35].

* daihan@ustc.edu.cn

† pan@ustc.edu.cn

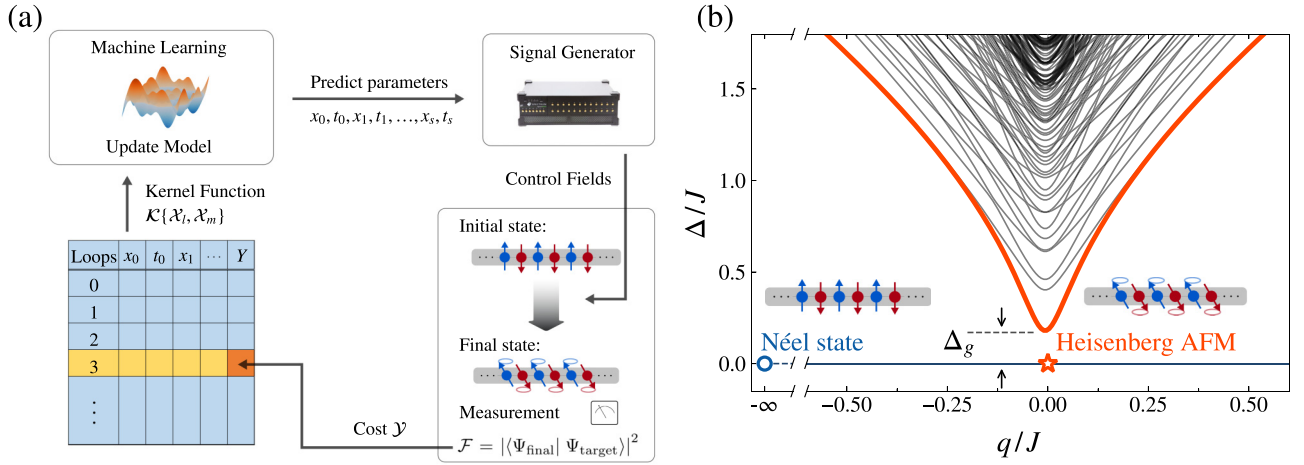


FIG. 1. The AFM preparation assisted by GPR. (a) The general scheme for a single GPR loop. (b) Ground-state passage in the 1D Heisenberg chain to the AFM. The dynamical evolution starts from the Néel state (circle) in a strong field and ends in an AFM (star). The solid lines are the energy levels for finite chain length $L = 20$ (thick line: the gap between the ground state and the first excited state). Δ_g is the energy gap between the ground state and the first excited state when the external field $q = 0$.

Compared to other machine learning methods, such as support vector machines [36] and neural networks [37], GPR is expected to be more feasible to experimental implementation, as it requires a relatively smaller training data set, especially in solving the optimizing problem with few dozens of control parameters [38,39]. Moreover, folding noise into the kernel function, one can accommodate different instabilities in experiments [40]. This algorithm has been recently used to optimize the creation of Bose-Einstein condensate in cold-atom experiments [41,42].

In this work, we implement the GPR algorithm to optimize scalable quantum many-body states with ultracold atoms in optical lattices. First, we simulate the preparation process of the bosonic Heisenberg antiferromagnet (AFM) state in a spin-1/2 chain [43–45] with matrix product states (MPSs) [46]. By maximizing the fidelity of the final state to the many-body ground state, the GPR algorithm produces sweeping profiles of the control fields by which the one-dimensional (1D) AFM state preparation fidelity reaches above 96%. Then, we utilize the transferability of the optimization tasks to apply a multistep learning strategy, further improving the scalability of our method. Compared to the traditional methods, such as the differential evolution (DE) and the Nelder-Mead (NM) method, our method shows greater robustness against noise. Afterward, we extend the algorithm to a square lattice and successfully achieve a two-dimensional (2D) AFM in favorable experimental settings. Finally, in optimizing the Hamiltonian ramping sequence across a quantum phase transition in an XXZ spin chain, we obtain an efficient protocol for creating the highly entangled Greenberger-Horne-Zeilinger (GHZ) state. In this regard, we conclude that GPR is a practical machine learning tool for optimal control of quantum many-body states.

II. OPTIMIZING WITH SUPERVISED LEARNING

We focus on the optimization problems in a class of quantum many-body dynamics. The quantum system is prepared

from an initial state $|\Psi_0\rangle$ through a dynamical control field \mathcal{X} into a final state $|\Psi_{\text{final}}\rangle$. As sketched in Fig. 1, we use the GPR algorithm based on the online policy [47], which is convenient for experiments, to perform optimization tasks. We first generate m sets of control fields $\{\mathcal{X}_1, \mathcal{X}_2, \dots, \mathcal{X}_m\}$ randomly. The corresponding costs $\{\mathcal{Y}_1, \mathcal{Y}_2, \dots, \mathcal{Y}_m\}$ are derived from numerical simulations or laboratory experiments. Next, these fields and costs are sent into the GPR as the initial training set. The algorithm will build a probabilistic model between the control fields and costs based on the kernel function $\mathcal{K}\{\mathcal{X}_i, \mathcal{X}_m\}$ [48]. Afterward, it will predict the smallest cost with an optimal control field \mathcal{X}_{m+1} . Then, the corresponding cost \mathcal{Y}_{m+1} is obtained from the final state, and the probabilistic model is updated. Following this regression loop, the optimization is achieved by gradually decreasing the cost. For convenience, we define the cost function of the control fields with the infidelity to the target state $\mathcal{Y} = 1 - \mathcal{F}$, $\mathcal{F} = |\langle \Psi_{\text{final}} | \Psi_{\text{target}} \rangle|^2$. We can also choose other observables for the cost functions according to the properties of the target state, such as the energy $E(|\Psi_{\text{final}}\rangle)$ for preparing a ground state [48].

In this work, we choose the control field with a piecewise linear function for experimental feasibility,

$$X(t) = \frac{x_i - x_{i-1}}{t_i - t_{i-1}}(t - t_{i-1}) + x_{i-1}, \quad t_{i-1} \leq t < t_i, \quad (1)$$

with $i = 0, 1, \dots, s$ (s is the segment number). Therefore, the control field can be represented by a set of parameters $\mathcal{X} = \{t_0, x_0, t_1, x_1, \dots, t_s, x_s\}$. In the following sections, we set segment number $s = 4$, and the dimension of the parameters is 10–12 for different constraints, which is very suitable for the GPR. The initial field is $t_0 = 0$, $x_0 = x_{\text{start}}$, and the ending field is $t_s = \tau$, $x_s = x_{\text{end}}$. These control parameters will be updated during the regression loops. It should be noted that the control fields can be described with interpolated splines or other designed continuous functions.

III. OPTIMIZING HEISENBERG ANTIFERROMAGNETS IN OPTICAL LATTICES

In this section, we apply the GPR method to optimize the dynamical evolution to prepare bosonic AFMs in a spin-1/2 Heisenberg chain. The system was realized in our recent experiments [45] and can be described by the spin-exchange interactions and a staggered external field,

$$H(t) = J \sum_{(i,j)} \mathbf{S}_i \mathbf{S}_j + q(t) \sum_i (-1)^i S_i^z, \quad (2)$$

where $\mathbf{S}_i = \{S_i^x, S_i^y, S_i^z\}$ are the spin operators on the i th site, L is the length of the lattice chain, $J > 0$ describes the spin-exchange interaction between nearest neighbors, and $q(t)$ is the time-dependent staggered longitudinal field. At zero temperature, this model hosts a global SU(2) spin-rotation symmetry. It can be solved with the exact methods for finite systems of $L \lesssim 20$, as shown in Fig. 1(b). In the thermodynamic limit, the energy gap Δ_g tends to be closed with $\Delta_g \propto 1/L$ [49]. Another interesting feature of this system is the ground state, which is the Néel state in the strong staggered field (i.e., $|q| \gg J$) and becomes the Heisenberg AFM at zero field, $q(t) = 0$.

In the experiment [45], we can easily initialize the system in high field to the Néel state $|\uparrow\downarrow\uparrow\downarrow \dots \uparrow\downarrow\rangle$ with the spin-dependent site-resolved addressing method [50]. Followed by a designed passage for the fields of $q(t)$ and $J(t)$ in the spin chain, the antiferromagnetic correlations are built up, and the spin-rotation symmetry is successfully probed. However, numerical simulations show that the AFMs remain imperfect due to the nonadiabaticity of the fields. To improve this ground-state passage, one must carefully find out an optimized path for the control fields to achieve the AFMs.

Here, we use MPSs to derive the antiferromagnetic ground state of a finite system and simulate its dynamical evolutions with the TEBD method [46]. The bond dimensions are set to $D = 200$ after checking the convergence of the simulations. A set of typical experimental parameters is considered, with a staggered field $q(t)$ of $h \times (0-25)$ Hz and spin-exchange interaction $J(t)$ of $h \times (0.2-26)$ Hz, and both of the control fields are parametrized with four linear segments by Eq. (1). For a demonstration of optimizing with GPR, we first take the case of $L = 80$ and duration $\tau = 800$ ms, in which the timescale is comparable to current ultracold-atom experiments [51]. As shown in Fig. 2(a), the cost Y converges quickly, which gives a state fidelity of 96.2% in 432 loops and 97.1% in 1000 loops. Thus, we successfully achieve the AFM with optimized fidelity, which is higher than the protocol in the XXZ spin chain [52]. The ramping rate of optimized fields slows down when approaching the critical region, where the energy gap tends to be closed. It is in agreement with the local-adiabaticity (LA) approach [53]. The spin correlations of the output state can be derived as

$$C_d = \frac{1}{N_d S^2} \sum_{i,j,d=i-j} \langle S_i^z S_j^z \rangle - \langle S_i^z \rangle \langle S_j^z \rangle, \quad (3)$$

with N_d being the number of different two-point lattice sites separated by a distance d . The typical power-law-type spin correlations for the optimized state are derived [shown in

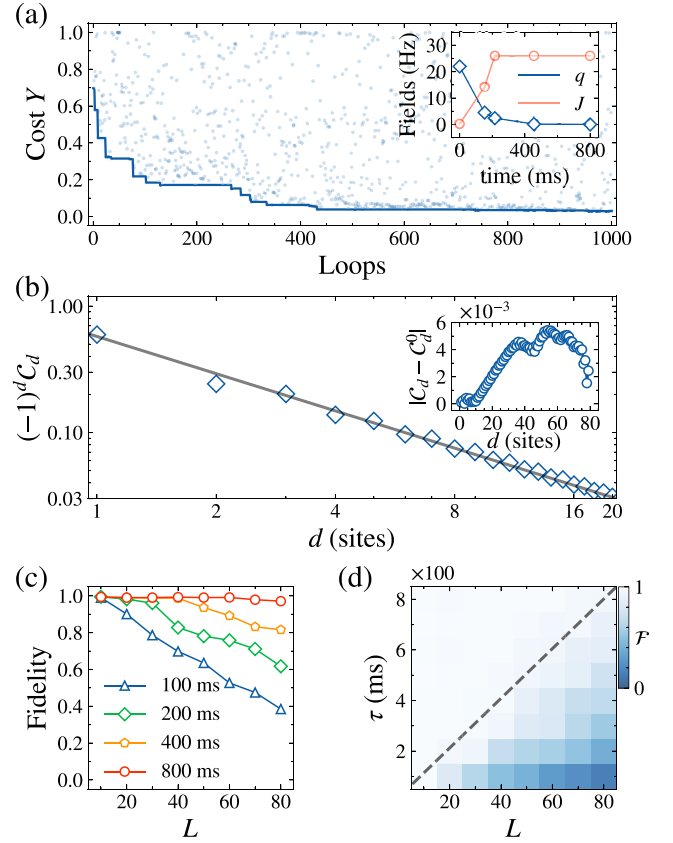


FIG. 2. Optimizing the preparation of 1D Heisenberg AFMs. (a) Optimization process for $L = 80$, $\tau = 800$ ms. Each dot is the measured cost in a single loop. Inset: the optimized sweeping profiles of staggered field $q(t)$ (blue diamonds) and the spin-exchange interaction $J(t)$ (red circles) after 1000 loops. The markers indicate the parametrized control fields at different time points (q_i, J_i, t_i). (b) Spin correlations C_d for the optimized fields (diamonds). The line is the fitting curve with the power-law function. The inset shows the difference of the correlation functions between the final state (C_d) and antiferromagnetic ground state (C_d^0). (c) and (d) Optimized fidelities for increased chain lengths L and ramping times τ . The color bar is in the parabolic scale.

Fig. 2(b)], where the nearest-neighbor (NN) and next-nearest-neighbor spin correlations achieve $C_1 = -0.595$ and $C_2 = 0.243$, respectively. They are stronger than the experimentally measured results in the Fermi-Hubbard model with $C_1 < -0.1$ [54]. The strong correlations are very close to the AFM ground states, indicating the establishment of entanglement among the spin chain. Next, we analyze the preparation of 1D AFMs for different chain lengths L and evolution time τ , as shown in Fig. 2(c). By increasing the ramping time, the output fidelity to the AFM gets larger and converges with $\mathcal{F} > 96\%$, proving the validity of our method. Meanwhile, the expenditure of time is on the order of the quantum speed limit [55], which is predicted to be $\tau \propto h/\Delta_g \propto L$ [dashed line in Fig. 2(d)]. Compared to the previous proposal using linear ramping curves, the required time to maintain the adiabaticity scales as $\tau \propto L^2$ [43]. Hence, our method may effectively save the time cost to realize scalable quantum many-body states [56].

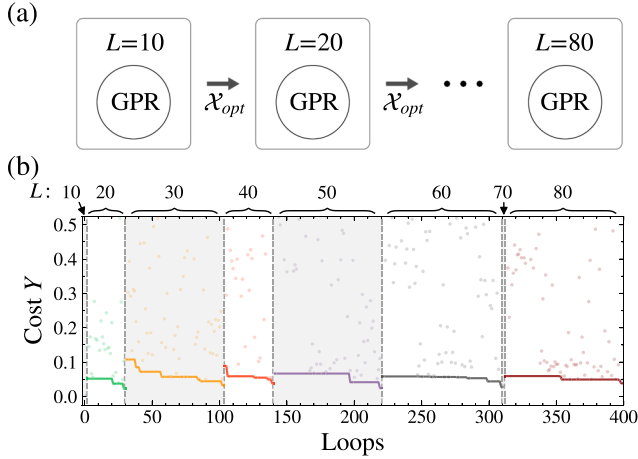


FIG. 3. The scalability of the GPR method. (a) The scheme of a multistep learning strategy. The optimized field \mathcal{X}_{opt} is transferred step by step with increasing chain length from $L = 10$ to $L = 80$. The GPR builds the training set with the derived costs from several fields around \mathcal{X}_{opt} to optimize a long chain. (b) Optimization process of multistep learning strategy for $\tau = 800$ ms. The area enclosed by the dashed lines represents the learning process for different chain lengths. Each dot is the measured cost in a single loop.

An important aspect for implementing the algorithm is the resource cost, especially when optimizing large systems. For example, the optimization task for $L = 80$ and $\tau = 800$ ms takes about 74 h to reach 96% state fidelity on a commercial computer (Intel i9-10900X@3.7GHz processor). The time cost is mainly for calculating the time evolution of MPSs, which almost scales with the system size, limiting further scaling of the system size. Taking advantage of the transferability of the GPR, we implement a multistep learning strategy for a large system, which gradually finds the approximate hyperparameters and a good initial curve from a small system. Specifically, from the completed tasks, where the state fidelity $\mathcal{F} \geq 96\%$, the optimized fields and the hyperparameters of the kernel function are subsequently forwarded to the training process for a longer chain, as shown in Fig. 3(a). Following this strategy, we consecutively optimize the AFMs of different chain lengths from $L = 10$ to 80. With the increasing chain length, we repeat 1, 29, 73, 37, 80, 90, 1, and 88 training loops [see Fig. 3(b)]. To analyze the efficiency of the multistep strategy, we compare its time costs with the direct learning method [48]. For a small system ($L < 40$), the time costs of the two strategies are similar. However, for a large system ($L > 40$), the efficiency of the multistep strategy is apparently shown. Especially, the total time cost for $L = 80$ is 49 h, which is a decrease of about 33%. Hence, combined with such a multistep learning strategy, it will enhance the potential scalability of our method for large system sizes.

IV. OPTIMIZING AGAINST NOISES

Next, we benchmark the performance of the GPR with the other two optimal control methods, the NM algorithm based on the direct search method [57] and the DE based on an evolution method [58]. For a clean chain with $L = 20$ and $\tau = 150$ ms [shown in Fig. 4(a)], the GPR method reaches

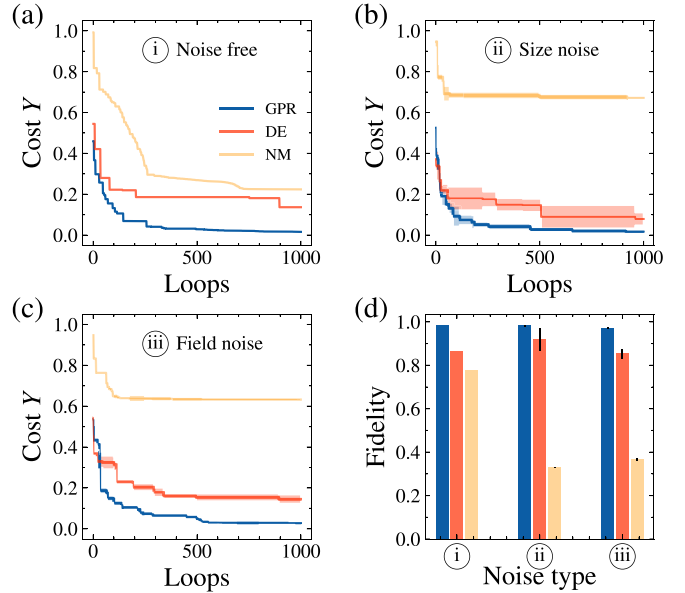


FIG. 4. A comparison among different optimization methods, including the GPR [blue (dark gray)], the DE [red (medium gray)], and the NM [yellow (light gray)]. (a)–(c) Convergence processes in the cases of no noise, system-size noise, and field noise, respectively. The solid lines are the convergence curves of the mean infidelities of every five simulations, while the shaded areas represent the statistical errors. (d) A comparison of the mean fidelities after 1000 GPR loops.

a ground-state fidelity of 98.4% in 1000 loops, while it is 86.3% for DE and 77.6% for NM. It shows that the machine learning method is potentially more efficient than the other two methods for multivariable optimizing tasks. Moreover, considering systematic noises of experiments, such as fluctuations of the system size [59] and Gaussian noises of control fields, will lead to the failure of some traditional optimal control methods [24,25]. However, these noises will be folded into the probabilistic model in GPR.

For example, we consider the noise of the system size caused by the particle-hole excitations in optical lattices at finite temperature. More specifically, the chain length in each run of the simulation is randomly picked from $L \in \{16, 18, 20, 22, 24\}$; that is, there is a uniform noise of $\delta_L = 4$ for a system of $\langle L \rangle = 20$. We choose a system size with even numbers to conserve zero magnetization. In this model, we use the mean infidelity of every five runs of the simulation for the cost function, $Y = 1 - \bar{\mathcal{F}}$. As shown in Fig. 4(b), the GPR and DE methods can still converge quickly with fluctuating system sizes and achieve state fidelities of $\mathcal{F} = 98.2\% \pm 0.4\%$ and $92.1\% \pm 5.1\%$, respectively. In contrast, the NM method gives a reduced final-state fidelity of $\mathcal{F} = 32.8\% \pm 0.2\%$. This shows that the NM method is susceptible to system-size noises, which strongly depend on the temperature of the system.

Another typical noise in the laboratory is the noises in control fields. We assume that they are typical Gaussian noises,

$$J_n(t) = J(t)[1 + \epsilon_1(t)], \quad q_n(t) = q(t)[1 + \epsilon_2(t)], \quad (4)$$

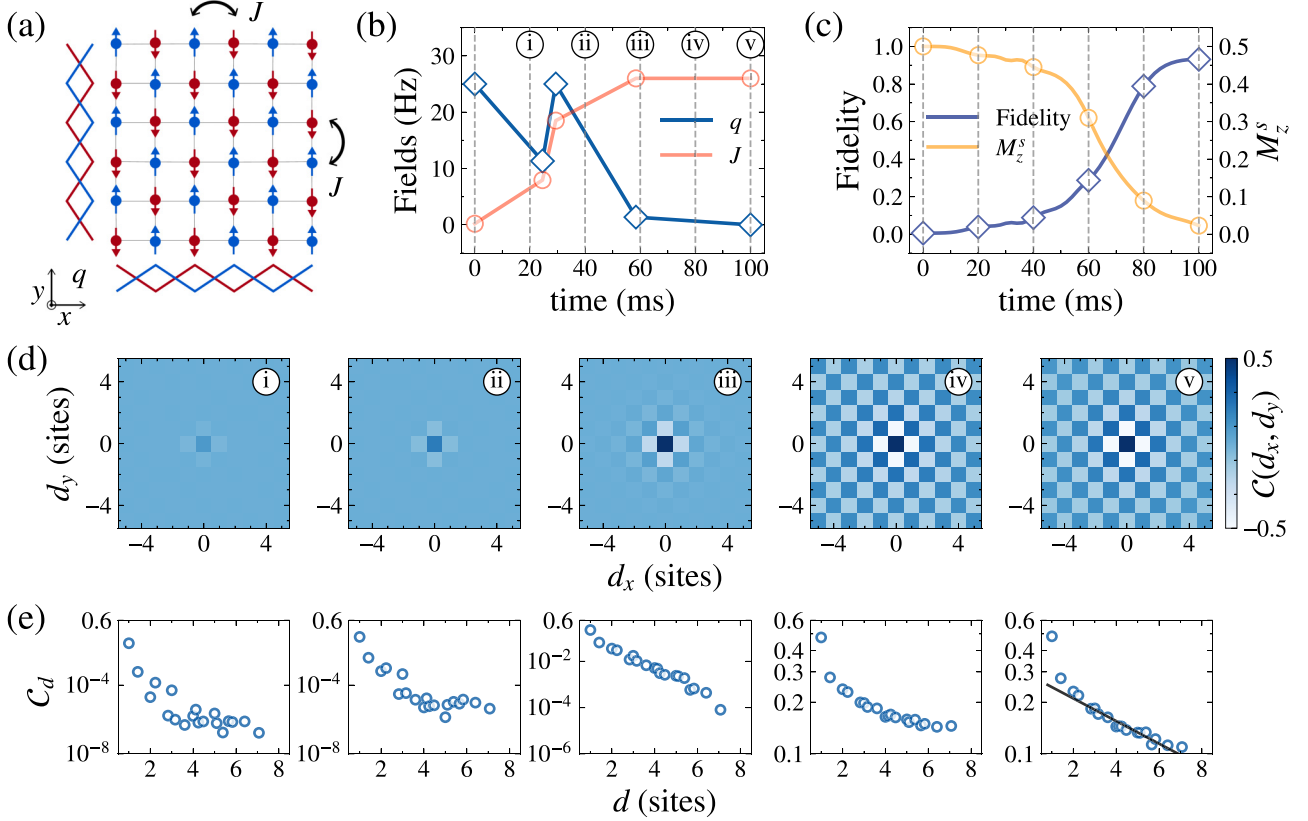


FIG. 5. The preparation of AFMs in a 2D optical lattice by GPR. (a) The 2D lattice configuration (6×6) in the staggered field. (b) The optimized sweeping profiles of the staggered field $q(t)$ (blue diamonds) and the spin-exchange interaction $J(t)$ (red circles). The markers indicate the parametrized control fields at different times (q_i, J_i, t_i). (c) The evolutions of fidelity \mathcal{F} (dark blue diamonds) and staggered magnetization M_z^s (yellow circles) for the optimized fields in a square lattice. (d) The establishment of the spin correlation. The correlator $\mathcal{C}(d_x, d_y)$ of the final state for different displacements shows antiferromagnetic order. (e) The correlation function C_d after the azimuthal average. The line is the exponential fit to the data (circles) of the final state for $|d| > 2$ sites.

where $\epsilon_{1,2}(t) \sim \mathcal{N}(0, \sigma^2)$ follows the normal distribution with mean amplitudes of zero and standard deviations of $\sigma = 10\%$. The convergence process is shown in Fig. 4(c), where the final-state fidelity for the GPR method reaches $97.1\% \pm 0.3\%$ after 1000 regression loops. However, it results in $85.3\% \pm 2.2\%$ for DE and $36.8\% \pm 0.6\%$ for NM. Hence, the GPR method is more resistant than the two traditional optimal control methods.

We note that other kinds of experimental constraints can be studied with our method as well, such as measurement noises, limited bandwidth of the driving fields, etc.

V. OPTIMIZING TWO-DIMENSIONAL HEISENBERG ANTIFERROMAGNETS

We further extend the machine-learning-assisted optimizing method into a more complex system, i.e., the 2D Heisenberg model on a square lattice with a staggered external field, where the target state becomes the 2D AFM. It plays an important role in simulating 2D magnetic materials [60], such as La_2CuO_4 . The system can be described by the following Hamiltonian:

$$H(t) = J(t) \sum_{\langle i,j \rangle} \mathbf{S}_i \mathbf{S}_j + q(t) \sum_{i_x, i_y} (-1)^{(i_x + i_y)} S_i^z, \quad (5)$$

where $\langle i, j \rangle$ are the nearest-neighbor sites on a square lattice with a size of $n_x \times n_y$, where $n_{x,y}$ are the sizes in the x and y directions and $i_{x,y}$ are the coordinates of the i th site. The lattice constant is a . As shown in Fig. 5(a), the dynamical field is along the diagonal direction, where the staggered field strength is $q(t)$ in both the x and y axes. Similar to the 1D case, the ground state of the system at high field is the Néel state, while at zero field it becomes the 2D AFM. The energy gap scales as $\Delta_g \propto (n_x \times n_y)^{-1}$ in the thermodynamic limit [49]. Therefore, one can also prepare 2D coherent many-body states through ground-state passages from Néel states to the 2D AFMs. At low temperature, the 2D Heisenberg model hosts antiferromagnetic correlations $\sim \exp(-d/\xi)$, with d being the distance between two sites and ξ being the correlation length [61].

For a demonstration, we optimize a finite 6×6 system with typical experimental parameters. The dynamical evolutions of the 2D system are implemented by the TDVP method [62]. Similar to the 1D case, the initial state is set to the Néel state in a large staggered field. Then, we optimize the control fields of $J(t)$ and $q(t)$ by GPR with a constrained evolution time of $\tau = 100$ ms and an initial staggered field of $h \times 25$ Hz. After 1000 regression loops, we achieve the 2D AFM ground state with a state fidelity of $\mathcal{F} = 94.0\%$. The corresponding control fields are shown in Fig. 5(b). The disappearance of

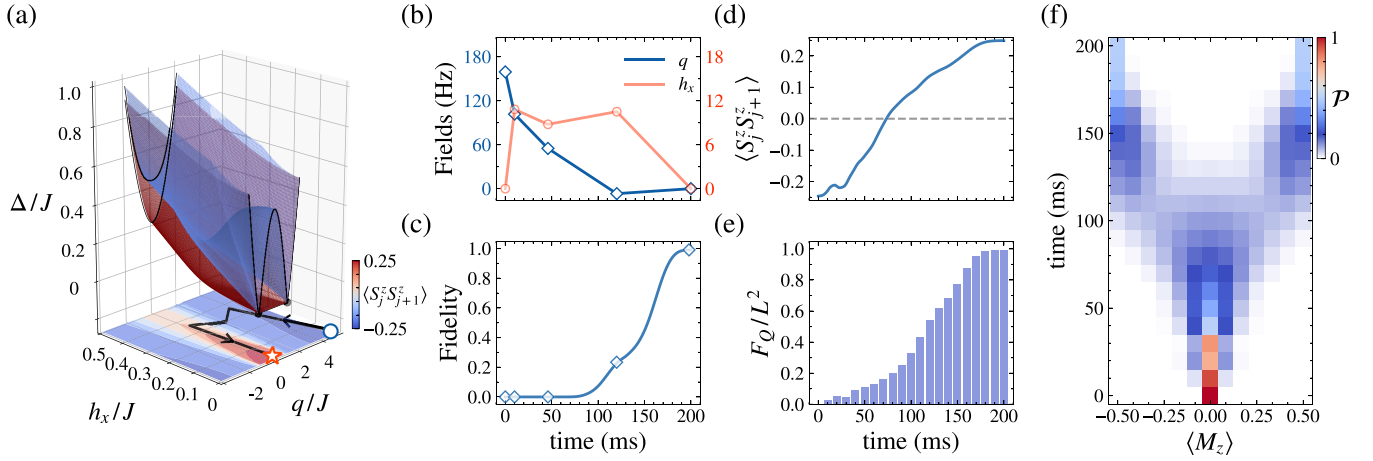


FIG. 6. The preparation of the GHZ state in a spin-1/2 XXZ chain for $L = 12$. (a) The energy levels of the XXZ chain in a staggered magnetic field q and a uniform field h_x . The normalized correlation $\langle S_j^z S_{j+1}^z \rangle$ of the ground state is plotted in the x - y plane, and the solid line is an evolutionary path from the Néel state (circle) to the GHZ state (star). The dots are the critical points where the energy levels of the ground state and the first excited state cross without a uniform field ($h_x = 0$). (b) The optimized sweeping profiles of $q(t)$ (blue diamonds) and $h_x(t)$ (red circles) for $\tau = 200$ ms. The markers indicate the parametrized control fields at different times (q_i, h_{xi}, t_i). (c) The optimized evolution of fidelity \mathcal{F} . (d) The dynamics of the spin correlations $\langle S_j^z S_{j+1}^z \rangle$ from the AFM phase to the FM phase. (e) The generation of quantum Fisher information F_Q from the Néel state to the GHZ state. (f) The instantaneous magnetization $\langle M_z \rangle$ by projection measurements. The color bar shows the measurement probabilities \mathcal{P} .

staggered magnetization $M_z^s = \sum_{i_x, i_y} (-1)^{(i_x + i_y)} S_i^z$ presents the spin dynamics from the Néel state to the AFM, as shown in Fig. 5(c). Then, we characterize the establishment of N -site antiferromagnetism with the spin correlator

$$\mathcal{C}(d_x, d_y) = \frac{1}{N(d_x, d_y) S^2} \sum_{d_x, d_y} \langle S_i^z S_j^z \rangle - \langle S_i^z \rangle \langle S_j^z \rangle, \quad (6)$$

where $N(d_x, d_y)$ is the number of two lattice sites i, j separated by the displacement (d_x, d_y) . As shown in Fig. 5(d), the state initially does not exhibit antiferromagnetic correlation. While entering into a critical region $q/J \ll 1$ at 60 ms, it first appears. The system finally arrives at a state with the spin correlations matching well with the 2D AFM. The correlation functions \mathcal{C}_d are calculated through the azimuthal average of the sign-corrected spin correlators $(-1)^{(i_x + i_y)} \mathcal{C}(d_x, d_y)$ for $d = \sqrt{d_x^2 + d_y^2}$ [see Fig. 5(e)]. The NN spin correlation \mathcal{C}_1 reaches 0.48, which is higher than the measured results of 0.3 in the experiments [61]. It exhibits an exponential scaling after fitting by exponential functions $\exp(-d/\xi)$ for long distance ($d > 2$) [63]. The final state reaches correlation length $\xi = 6.6a$, which matches the size of the full system. This proves that the optimized final state generates strong 2D antiferromagnetic order in the system.

VI. OPTIMIZING THE PREPARATION OF GHZ STATES

Moreover, we propose to generate the maximally entangled states in optical lattices via a machine-learning-optimized quantum phase transition. Specifically, we consider a 1D anisotropic spin-1/2 XXZ model in external fields, which breaks the spin-rotational symmetry. The system is strongly correlated at low temperature and hosts long-range orders in

spin correlations. It is described by the Hamiltonian

$$H(t) = -J \sum_{\langle i, j \rangle} [(S_i^x S_j^x + S_i^y S_j^y) + \delta S_i^z S_j^z] + \sum_i^L [q(t)(-1)^i S_i^z + h_x(t) S_i^x], \quad (7)$$

where $J > 0$ is the spin-exchange interaction, $\delta > 1$ is the anisotropic parameter, $q(t)$ describes a staggered longitudinal field, $h_x(t)$ describes a uniform transverse field, and L is the chain length. In experiment, one can introduce the anisotropy of spin interactions by varying the spin-dependent lattice potentials V_\uparrow and V_\downarrow [64]. Here, we set $\delta = 1.5$ [48]. One can solve the model with exact diagonalization methods for finite system sizes, e.g., $L = 12$ [shown in Fig. 6(a)]. The system size in this work is limited mainly by our computational resources.

For $q \gg J$ and $h_x = 0$, the ground state is a Néel state belonging to the antiferromagnetic phase, which is aligned by the staggered field. By decreasing the staggered field, the system crosses a quantum phase transition from antiferromagnetic to ferromagnetic with the closure of the energy gap, where the normalized correlation $\langle S_j^z S_{j+1}^z \rangle = \sum S_j^z S_{j+1}^z / (L)$ changes sign, as shown in Fig. 6(a). Especially, at $q = 0$ and $h_x = 0$, i.e., without any external field, the model elaborates \mathbb{Z}_2 symmetry, resulting in the ground states being a set of degenerate states of $\cos\theta |\uparrow\uparrow \dots \uparrow\rangle + e^{i\phi} \sin\theta |\downarrow\downarrow \dots \downarrow\rangle$. When $\theta = \pm\pi/4$, the ground state becomes the GHZ-type state. However, the gap-closure feature prevents us from achieving GHZ states by simply ramping down the staggered field. By introducing a finite transverse field h_x , the symmetry of the ground state will be broken, and a finite energy gap will be opened. Hence, one can find a path by carefully tuning

both $q(t)$ and $h_x(t)$ to prepare the GHZ state. Additionally, the system is in a gapped phase at zero external fields, protecting the GHZ states from perturbations.

As in the previous simulations, we set the Néel state as the initial state and a constraint of $q_{\text{end}} = 0$, $h_{\text{end}} = 0$ for the control fields. The spin-exchange interaction is set to a typical experimental parameter with $J = h \times 31.8$ Hz. Then, we start the GPR optimizations by simulating the evolutions through the Schrödinger equation. For an evolution time of $\tau = 200$ ms, we achieve a final-state fidelity of the GHZ state higher than 99%, as shown in Figs. 6(b) and 6(c). The optimized control fields drive the system to avoid the critical point and traverse the quantum phase transition. We characterize the phases by the spin correlation $\langle S_j^z S_{j+1}^z \rangle$, which changes sign from antiferromagnetic to ferromagnetic [see Fig. 6(d)].

The output state can be further estimated by a Ramsey experiment or the projection measurements [65]. Here, we investigate the generation of entanglement during the quantum phase transition by introducing the quantum Fisher information [66],

$$F_Q(|\Psi\rangle, \hat{R}) = 4(\Delta \hat{R})^2, \quad (8)$$

where $\hat{R} = \vec{n} \cdot \vec{M}$, \vec{n} is the interferometric direction, and $\hat{M}_k = \sum_i^L S_i^k$ is the sum of all the spins along $k = x, y, z$. As shown in Fig. 6(e), the initial Néel state is a product state with zero Fisher information. The entanglement is gradually built up in the system through the optimized control fields. In the end, it arrives at the GHZ state with $F_Q/L^2 \approx 1$, i.e., approaching the Heisenberg limit. One can also measure the magnetizations $\langle i|M_z|i\rangle$ during the evolution; $|i\rangle$ is the eigenstate of the instantaneous Hamiltonian. The total magnetization $\sum \langle i|M_z|i\rangle$ is always kept at zero for the whole process. However, the distribution of magnetizations by the projection measurements shows a clear transition from a single peak at zero to a binary distribution at ± 0.5 , as shown in Fig. 6(f).

VII. SUMMARY

In summary, we applied the Bayesian learning method based on GPR to optimize the coherent quantum many-body ground state via numerical simulations. With the optimized control fields of spin interactions and staggered external fields, we obtained efficient Hamiltonian ramping sequences in preparing correlated ground states of 1D and 2D spin-1/2 Heisenberg models and produced high-quality antiferromagnetic states in our numerical simulation. By integrating a multistep learning strategy in the GPR method, we demonstrated its scalability from relatively small to large systems. By considering different noise channels that are relevant to optical lattice experiments, the machine-learning-assisted optimal control method exhibits significant robustness, which is crucial for laboratory implementation. We extend this method to an anisotropic XXZ model, where the maximally entangled GHZ state is generated by crossing a quantum phase transition from antiferromagnetic to ferromagnetic. Since the examined models and the parameter regions in our numerical simulations are directly from the ongoing optical lattice experimental setups, the results help clarify the nonadiabaticity in the experiments [45] and provide important guidance for further improvement.

ACKNOWLEDGMENTS

We thank L. Pezze for the helpful discussions. This work was supported by the National Natural Science Foundation of China (Grants No. 12074367 and No. 11625522), the Fundamental Research Funds for the Central Universities, the Anhui Initiative in Quantum Information Technologies, the Program of Shanghai Academic/Technology Research Leader (Grant No. 18XD1404000), the National Key Research and Development Program of China (Grants No. 2020YFA0309804 and No. 2018YFA0306501), the Shanghai Municipal Science and Technology Major Project (Grant No. 2019SHZDZX01), and the Chinese Academy of Sciences.

-
- [1] M. A. Nielsen and I. L. Chuang, *Quantum Computation and Quantum Information* (Cambridge University Press, Cambridge, 2000).
 - [2] C. H. Bennett and D. P. DiVincenzo, *Nature (London)* **404**, 247 (2000).
 - [3] R. Islam, R.-Ch. Ma, P. M. Preiss, M. E. Tai, A. Lukin, M. Rispoli, and M. Greiner, *Nature (London)* **528**, 77 (2015).
 - [4] P. Jurcevic, B. P. Lanyon, P. Hauke, C. Hempel, P. Zoller, R. Blatt, and C. F. Roos, *Nature (London)* **511**, 202 (2014).
 - [5] A. Manchon, J. Železný, I. M. Miron, T. Jungwirth, J. Sinova, A. Thiaville, K. Garello, and P. Gambardella, *Rev. Mod. Phys.* **91**, 035004 (2019).
 - [6] I. Bloch, J. Dalibard, and W. Zwerger, *Rev. Mod. Phys.* **80**, 885 (2008).
 - [7] M. Cheneau, P. Barmettler, D. Poletti, M. Endres, P. Schauß, T. Fukuhara, C. Gross, I. Bloch, C. Kollath, and S. Kuhr, *Nature (London)* **481**, 484 (2012).
 - [8] H. Weimer, A. Kshetrimayum, and R. Orús, *Rev. Mod. Phys.* **93**, 015008 (2021).
 - [9] X.-Y. Luo, Y.-Q. Zou, L.-N. Wu, Q. Liu, M.-F. Han, M. K. Tey, and L. You, *Science* **355**, 620 (2017).
 - [10] Y.-A. Chen, X.-H. Bao, Z.-S. Yuan, S. Chen, B. Zhao, and J.-W. Pan, *Phys. Rev. Lett.* **104**, 043601 (2010).
 - [11] L. S. Brown and G. Gabrielse, *Rev. Mod. Phys.* **58**, 233 (1986).
 - [12] T. Monz, P. Schindler, J. T. Barreiro, M. Chwalla, D. Nigg, W. A. Coish, M. Harlander, W. Hänsel, M. Hennrich, and R. Blatt, *Phys. Rev. Lett.* **106**, 130506 (2011).
 - [13] X.-L. Wang, L.-K. Chen, W. Li, H.-L. Huang, C. Liu, C. Chen, Y.-H. Luo, Z.-E. Su, D. Wu, Z.-D. Li, H. Lu, Y. Hu, X. Jiang, C.-Z. Peng, L. Li, N.-L. Liu, Y.-A. Chen, C.-Y. Lu, and J.-W. Pan, *Phys. Rev. Lett.* **117**, 210502 (2016).
 - [14] C. Song, K. Xu, W.-X. Liu, C.-P. Yang, S.-B. Zheng, H. Deng, Q.-W. Xie, K.-Q. Huang, Q.-J. Guo, L.-B. Zhang, P.-F. Zhang, D. Xu, D.-N. Zheng, X.-B. Zhu, H. Wang, Y.-A. Chen, C.-Y. Lu, S.-Y. Han, and J.-W. Pan, *Phys. Rev. Lett.* **119**, 180511 (2017).

- [15] T. Hartke, B. Oreg, N.-Y. Jia, and M. Zwierlein, *Nature (London)* **601**, 537 (2022).
- [16] P. Král, I. Thanopoulos, and M. Shapiro, *Rev. Mod. Phys.* **79**, 53 (2007).
- [17] P. Doria, T. Calarco, and S. Montangero, *Phys. Rev. Lett.* **106**, 190501 (2011).
- [18] N. Khaneja, T. Reiss, C. Kehlet, T. Schulte-Herbrüggen, and S. J. Glaser, *J. Magn. Reson.* **172**, 296 (2005).
- [19] E. Farhi, J. Goldstone, and S. Gutmann, [arXiv:1411.4028](https://arxiv.org/abs/1411.4028).
- [20] T. M. Graham *et al.*, *Nature (London)* **604**, 457 (2022).
- [21] H. Levine, A. Keesling, G. Semeghini, A. Omran, T. T. Wang, S. Ebadi, H. Bernien, M. Greiner, V. Vuletić, H. Pichler, and M. D. Lukin, *Phys. Rev. Lett.* **123**, 170503 (2019).
- [22] M. Jiang, J. Bian, X.-M. Liu, H.-Y. Wang, Y.-L. Ji, B. Zhang, X.-H. Peng, and J.-F. Du, *Phys. Rev. A* **97**, 062118 (2018).
- [23] D. Liang, L. Li, and S. Leichenauer, *Phys. Rev. Research* **2**, 033402 (2020).
- [24] T. Fösel, P. Tighineanu, T. Weiss, and F. Marquardt, *Phys. Rev. X* **8**, 031084 (2018).
- [25] J. H. Sørensen, M. K. Pedersen, M. Munch, P. Haikka, J. H. Jensen, T. Planke, M. G. Andreasen, M. Gajdacz, K. Mølmer, A. Lieberoth, and J. F. Sherson, *Nature (London)* **532**, 210 (2016).
- [26] G. Carleo, I. Cirac, K. Cranmer, L. Daudet, M. Schuld, N. Tishby, L. Vogt-Maranto, and L. Zdeborová, *Rev. Mod. Phys.* **91**, 045002 (2019).
- [27] I. Khait, J. Carrasquilla, and D. Segal, *Phys. Rev. Research* **4**, L012029 (2022).
- [28] É. Genois, J. A. Gross, A. D. Paolo, N. J. Stevenson, G. Koolstra, A. Hashim, I. Siddiqi, and A. Blais, *PRX Quantum* **2**, 040355 (2021).
- [29] V. V. Sivak, A. Eickbusch, H. Liu, B. Royer, I. Tsioutsios, and M. H. Devoret, *Phys. Rev. X* **12**, 011059 (2022).
- [30] M.-Y. Niu, S. Boixo, V. N. Smelyanskiy, and H. Neven, *npj Quantum Inf.* **5**, 33 (2019).
- [31] J. Lin, Z.-Y. Lai, and X.-P. Li, *Phys. Rev. A* **101**, 052327 (2020).
- [32] L. Banchi, N. Pancotti, and S. Bose, *npj Quantum Inf.* **2**, 16019 (2016).
- [33] R. Mukherjee, H. Xie, and F. Mintert, *Phys. Rev. Lett.* **125**, 203603 (2020).
- [34] S.-F. Guo, F. Chen, Q. Liu, M. Xue, J.-J. Chen, J.-H. Cao, T.-W. Mao, M. K. Tey, and L. You, *Phys. Rev. Lett.* **126**, 060401 (2021).
- [35] C. E. Rasmussen and C. K. I. Williams, *Gaussian Processes for Machine Learning* (MIT Press, Cambridge, MA, 2006).
- [36] A. Widodo and B.-S. Yang, *Mech. Syst. Signal Process.* **21**, 2560 (2007).
- [37] K. Gurney, *An Introduction to Neural Networks* (CRC Press, Boca Raton, FL, 2018).
- [38] S. Ba and V. R. Joseph, *Ann. Appl. Stat.* **6**, 1838 (2012).
- [39] J. Verrelst, L. Alonso, J. Rivera Caicedo, J. Moreno, and G. Camps-Valls, *IEEE J. Sel. Top. Appl. Earth Obs. Remote Sens.* **6**, 867 (2013).
- [40] J. Quiñonero-Candela and C. E. Rasmussen, *J. Mach. Learn. Res.* **6**, 1939 (2005).
- [41] P. B. Wigley, P. J. Everitt, A. D. Hengel, J. W. Bastian, M. A. Sooriyabandara, G. D. McDonald, K. S. Hardman, C. D. Quinlivan, P. Manju, C. N. Kuhn, I. R. Petersen, A. N. Luiten, J. J. Hope, N. P. Robins, and M. R. Hush, *Sci. Rep.* **6**, 25890 (2016).
- [42] E. T. Davletov, V. V. Tsyganok, V. A. Khlebnikov, D. A. Pershin, D. V. Shaykin, and A. V. Akimov, *Phys. Rev. A* **102**, 011302(R) (2020).
- [43] M. Lubasch, V. Murg, U. Schneider, J. I. Cirac, and M. C. Banuls, *Phys. Rev. Lett.* **107**, 165301 (2011).
- [44] A. S. Sørensen, E. Altman, M. Gullans, J. V. Porto, M. D. Lukin, and E. Demler, *Phys. Rev. A* **81**, 061603(R) (2010).
- [45] H. Sun, B. Yang, H.-Y. Wang, Z.-Y. Zhou, G.-X. Su, H.-N. Dai, Z.-S. Yuan, and J.-W. Pan, *Nat. Phys.* **17**, 990 (2021).
- [46] G. Vidal, *Phys. Rev. Lett.* **93**, 040502 (2004).
- [47] A. Ranganathan, M.-H. Yang, and J. Ho, *IEEE Trans. Image Process.* **20**, 391 (2010).
- [48] See Supplemental Material at <http://link.aps.org/supplemental/10.1103/PhysRevA.106.013316> for the details on implementing the optimization method and the cost function, discussions of adiabaticity, realization of XXZ model in optical lattice, and the calculation of the quantum fisher information.
- [49] S. R. White, R. M. Noack, and D. J. Scalapino, *Phys. Rev. Lett.* **73**, 886 (1994).
- [50] B. Yang, H.-N. Dai, H. Sun, A. Reingruber, Z.-S. Yuan, and J.-W. Pan, *Phys. Rev. A* **96**, 011602(R) (2017).
- [51] J. de Hond, J. Xiang, W. C. Chung, E. Cruz-Colón, W. Chen, W. C. Burton, C. J. Kennedy, and W. Ketterle, *Phys. Rev. Lett.* **128**, 093401 (2022).
- [52] S. Gammelmark and A. Eckardt, *New J. Phys.* **15**, 033028 (2013).
- [53] T. Albash and D. A. Lidar, *Rev. Mod. Phys.* **90**, 015002 (2018).
- [54] D. Greif, G. Jotzu, M. Messer, R. Desbuquois, and T. Esslinger, *Phys. Rev. Lett.* **115**, 260401 (2015).
- [55] T. Caneva, T. Calarco, R. Fazio, G. E. Santoro, and S. Montangero, *Phys. Rev. A* **84**, 012312 (2011).
- [56] P. Richerme, C. Senko, S. Korenblit, J. Smith, A. Lee, R. Islam, W. C. Campbell, and C. Monroe, *Phys. Rev. Lett.* **111**, 100506 (2013).
- [57] J. C. Lagarias, J. A. Reeds, M. H. Wright, and P. E. Wright, *SIAM J. Optim.* **9**, 112 (1998).
- [58] S. Das and P. N. Suganthan, *IEEE Trans. Evol. Comput.* **15**, 4 (2010).
- [59] M. Endres, H. Bernien, A. Keesling, H. Levine, E. R. Anschuetz, A. Krajenbrink, C. Senko, V. Vuletic, M. Greiner, and M. D. Lukin, *Science* **354**, 1024 (2016).
- [60] E. Manousakis, *Rev. Mod. Phys.* **63**, 1 (1991).
- [61] A. Mazurenko, C. S. Chiu, G. Ji, M. F. Parsons, M. K. Kanász-Nagy, R. Schmidt, F. Grusdt, E. Demler, D. Greif, and M. Greiner, *Nature (London)* **545**, 462 (2017).
- [62] J. Haegeman, J. I. Cirac, T. J. Osborne, I. Pižorn, H. Verschelde, and F. Verstraete, *Phys. Rev. Lett.* **107**, 070601 (2011).
- [63] E. V. Gorelik, D. Rost, T. Paiva, R. Scalettar, A. Klümper, and N. Blümer, *Phys. Rev. A* **85**, 061602(R) (2012).
- [64] L.-M. Duan, E. Demler, and M. D. Lukin, *Phys. Rev. Lett.* **91**, 090402 (2003).
- [65] R. Mukherjee, T. C. Killian, and K. R. A. Hazzard, *Phys. Rev. A* **94**, 053422 (2016).
- [66] L. Pezzè, A. Smerzi, M. K. Oberthaler, R. Schmied, and P. Treutlein, *Rev. Mod. Phys.* **90**, 035005 (2018).